ARTICLE

Laser induced molybdenum sulphide loading on doped graphene cathode for highly stable lithium sulphur battery

Yihe Huang[1], Richard Field[2], Qian Chen[2], Yudong Peng[2], Monika S. Walczak[3], Hu Zhao[2], Guangyu Zhu[4], Zhu Liu[2,1] & Lin Li[1]*

Lithium sulphur (Li-S) batteries are known to have much higher charge capacity than the currently widely used lithium-ion batteries with graphite anodes. However, maintaining high charge cycle stability is a key challenge for Li-S batteries due to the shuttle effect. Here we show highly stable characteristics with 100% charge capacity of Li-S batteries with 500 charge/discharge cycles at 0.5 C, 1 C, 2 C and 3 C charge rates. This was made possible by the combination of laser synthesised sulfur (S) and nitrogen (N) doped graphene electrodes (without a binder) with molybdenum sulphide (MoS_2) nanoparticle loading. The N/S doped porous graphene structure presented enhanced interface adsorption by the production of $-SO_2$, which suppressed diffusion of polysulfide into the electrolyte through promoting oxygen-containing functional groups chemically bonding with sulfur. A low electrolyte resistance, interphase contact resistance and charge-transfer resistance accelerate electrons and Li^+ transport by laser induced N/S doped graphene.

[1] Laser Processing Research Centre, Department of Mechanical, Aerospace and Civil Engineering, The University of Manchester, Manchester M13 9PL, UK. [2] Department of Materials, The University of Manchester, Manchester M13 9PL, UK. [3] School of Chemical Engineering and Analytical Science, The University of Manchester, Manchester M13 9PL, UK. [4] Electronic and Electric Engineering School, Chongqing University of Arts and Sciences, Chongqing, China. *email: lin.li@manchester.ac.uk

The demand for efficient, durable, and lightweight energy storage systems increases rapidly in recent years due to the growing need for electrical vehicles and portable electronic devices, such as mobile phones and laptop computers. Lithium ion batteries are currently dominating the market for the above uses[1,2]. Graphite and graphene are widely used as an anode material in lithium ion batteries, based on intercalation chemistry. However, the theoretical maximum specific capacity of the graphite or graphene based Li-ion batteries is about 372 mAh/g that cannot meet growing customer needs[3–5]. Lithium sulfur (Li–S) batteries have a very high theoretical specific capacity of 1675 mAh/g and a relatively higher theoretical energy density of 2600 Wh/kg, which offer a potential candidate among various alternatives for the battery of the future[6]. Although energy density of 550–600 Wh/kg is a target for practical Li–S batteries, which is 20% of the theoretical energy density based on mass calculation, this level of energy density has been achieved in commercial Li-ion battery with a $LiCoO_2$ cathode[7]. Therefore achieving high volumetric energy density of Li–S battery is one of the primary challenges. Low cycle stability is also hindering practical application of Li–S battery. The soluble lithium polysulfide is the key factor of the "shuttle" effect in electrochemical reaction on the sulfur cathode. It induced low cycle stability from the loss of sulfur to electrolyte[8]. The most common strategy to overcome this includes physically confining sulfur in various carbon materials and organics. The carbon materials, such as meso- or microporous carbon[9], carbon nanotubes[10], carbon fiber[11], reduced graphene oxide[12], and carbon sphere[13], can provide desirable electrical properties for electron transfer to the current collector, space for sulfur loading and volume expansion compensation during lithiation and delithiation[14,15]. However, polysulfide dissolves in electrolyte through the interconnected space of these carbon materials. Instead of polysulfide diffusion, the limited pore volume reduces sulfur loading content by decreasing the pore size[16,17]. Pure carbon materials offer a weak interaction toward polar lithium polysulfide against the long-term cycle stability of sulfur cathode. The inverse vulcanized polymers, such as styrenics[18], alkynes[19], naturally occurring/commercial olefins[20], allylics[21], oleyamine[22], aliphatic amines[19], allylethers, maleimide[23], nitriles, and benzoxazines[22], can also confine sulfur in crosslinked organic structures. The rigidity of organic materials

with aromatic group induced a vulcanized structure after long-term charge and discharge cycles; therefore the fading rate for each cycle is difficult to be kept above 80% capacity after long cycle times. The heteroatom modification of carbon hosts was utilized to enhance the affinity and catalytic conversion of intermediate Li_nS[24].

In recent studies, sulfur was fastened by polar compounds, such as metal oxides[25], sulfide[26], nitrides[27], carbides[28], phosphides, and MXene[29] to improve the cycle stability through polar interaction between polar compounds and Li_nS. The polar compounds can also accelerate the catalytic conversion kinetics of intermediate Li_nS, which is beneficial to reducing the sulfide accumulation and shuttle effect[30,31].

Here, we show a pulsed UV laser direct writing technique to form S and N doped graphene electrodes with various nanoparticles loading, such as silver, platinum, silicon, and molybdenum sulfide from a specially formulated organic ink with various microparticles. This technique is a one-step fabrication process without a binder to form a current collector for lithium sulfur battery cathodes. The process enables long-term cycles with almost no fading in charge capacities.

Results

Surface morphology and Raman spectra of laser-induced cathodes. As the Raman spectra mapping shown in Fig. 1, a heteroatom (N and S) doped porous graphene was synthesized from a specially formulated polybenzimidazole (PBI) ink through a one-step laser direct writing technique[32].

Molybdenum trisulfide microparticles were mixed in the PBI ink and coated on a 20 µm aluminum foil current collector. The decrease of the mean value $I(2D)/I(G)$ about 0.5 and the increase of mean $I(D)/I(G)$ about 0.8 in Fig. 1, compared with that of graphene from pure PBI ink[32], demonstrated a reasonable low impact from the specific particle additions. As shown from the white metallic spots in the back-scattered electrons image in Fig. 2a, a 0.27 nm interplanar space periodic pattern was formed in the lattice fringe image shown in Fig. 2d and molybdenum, sulfur element mapping from energy dispersive spectra image shown in Fig. 2c showed a high volume ratio of nano-MoS_2 with 160.07 g/mol (45%) calculated from MoO_3 with 143.95 g/mol in
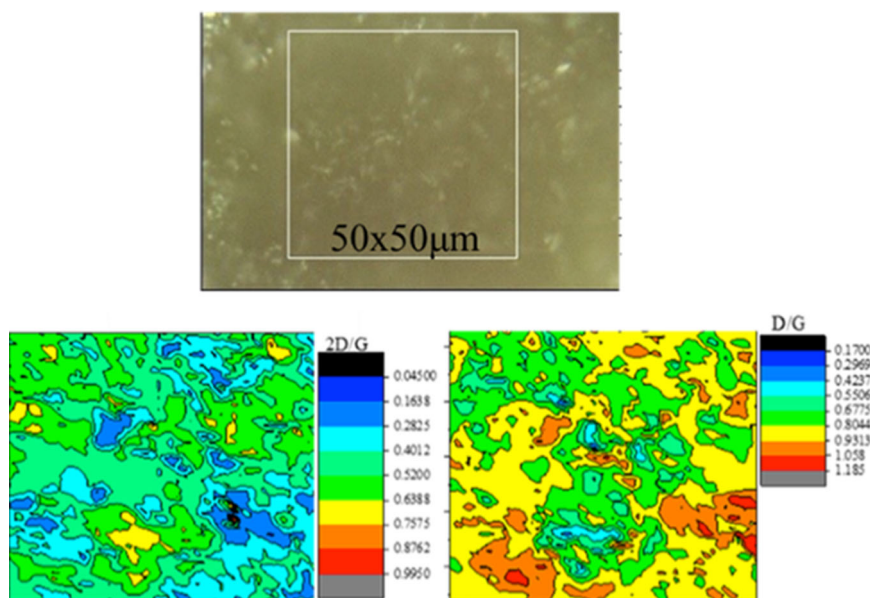
Fig. 1 Surface characterization. Raman spectra mapping of the heteroatom doped porous graphene with molybdenum sulfide (MoS_2) nanoparticle implant.
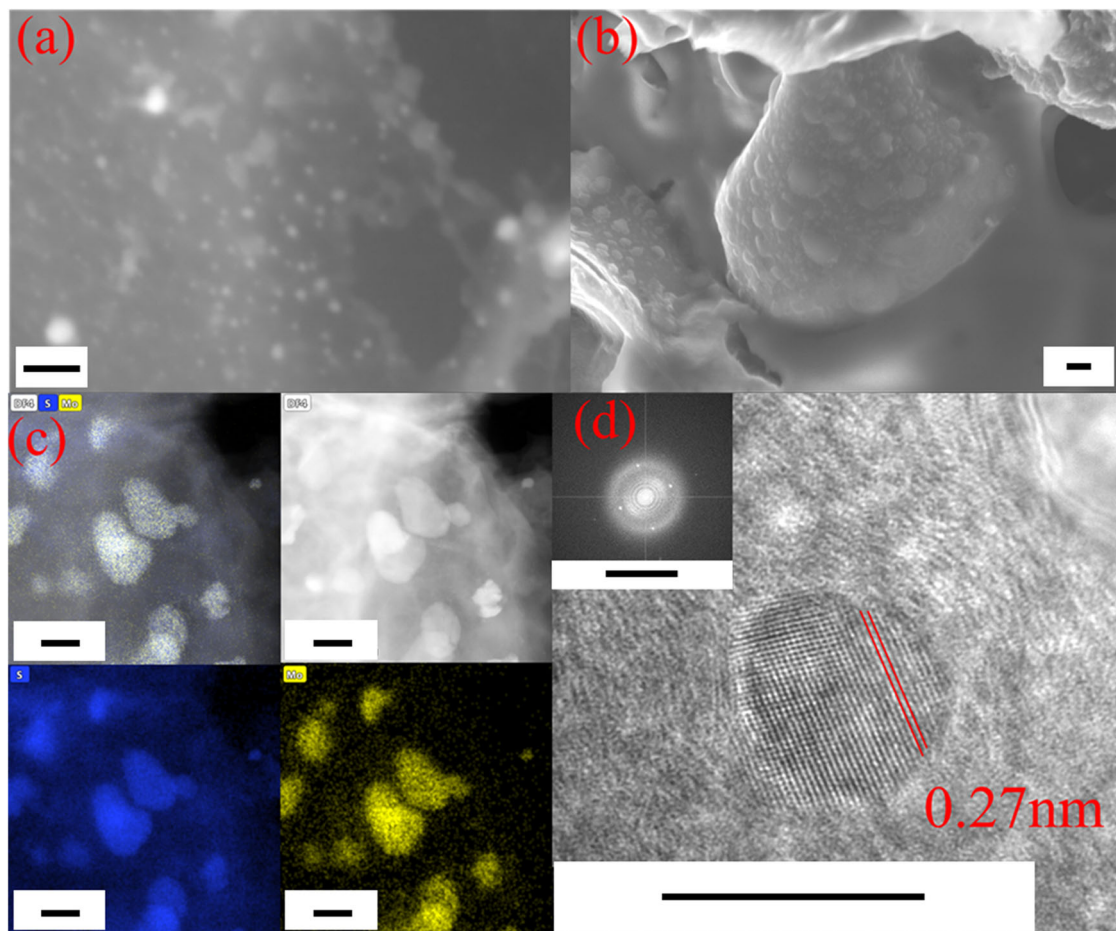
Fig. 2 Surface morphology and elementary distribution of nano-molybdenum disulfide loading in graphene. a BSE image from SEM before cross-linked sulfur loading. **b** Inlens image from SEM. **c** STEM-EDS image (scale bar: 200 nm) after cross-linked sulfur loading (scale bar: 50 nm) and **d** HRTEM image (scale bar:100 nm) before cross-linked sulfur loading.
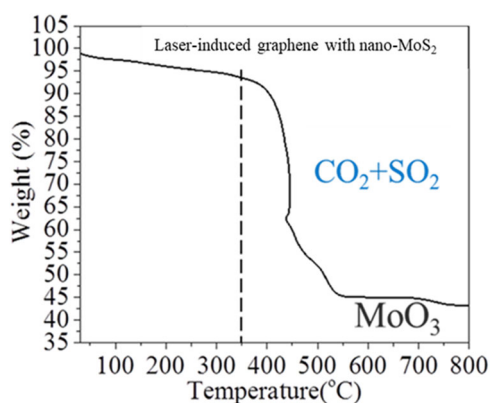
Fig. 3 Thermo-gravimetric analysis. Thermo-gravimetric analysis of the heteroatom doped porous graphene with molybdenum sulfide (MoS_2) nanoparticle under ambient condition (eventual product includes: carbon dioxide (CO_2), sulfur dioxide (SO_2), and molybdenum trioxide (MoO_3).

Fig. 3 with a wide range of 10–50 nm to functionalized the graphene structure.

As the 355 nm UV laser wavelength has a photon energy of 3.49 eV, which is higher than the C–S bond energy (2.8 eV) from the dimethyl sulfoxide (DMSO) (a component of the PBI ink) and the C–N bond energy (3.14 eV) of PBI, it would enable both photochemical and photothermal processes to occur when interacting with the PBI ink to enable customized sulfur and

nitrogen doping at low laser powers and avoid thermal damages to the substrate[33–35]. The 10 ps pulse length induced ablation effect on the micro particles, which resulted in the in-situ production of nanoparticles implanted in the doped graphene porous structure. The nanoparticles were formed from plasma aggregation and fastened to the graphene in recombination of the aromatic ring under self-generation gas protection from the PBI ink when the picosecond laser degraded and ablated the PBI ink. The experiment was carried out in ambient air. The recrystallization of material plasma, which was demonstrated from the lattice fringe image with 0.27 nm interlayer spacing and Fast Fourier transformation analysis in Fig. 2d and electron diffraction pattern for molybdenum disulfide in Fig. 2c separately, was resulted from high laser pulse energy and was prevented from oxidation by the production of carbon rings[36].

Lithium sulfur battery cathode preparation. In the sulfur cathode preparation, the heteroatom (N and S) doped graphene was grown both on aluminum foil directly for the cathode with nano-MoS_2 loading and was prepared into slurry with a water soluble binder (5%) for the cathode with micro-MoS_2 loading.

Compared with hydrophobic commercial graphene nanoparticles, the heteroatom doped graphene reported here showed a super-hydrophilic wettability with a 0º contact angle after 2.4 s spreading on surface shown in Fig. 4, due to low surface energy by functionalized N doping in pyrrolic structure originated from the PBI (7.5%) and the porous graphene structure[37]. The cross-
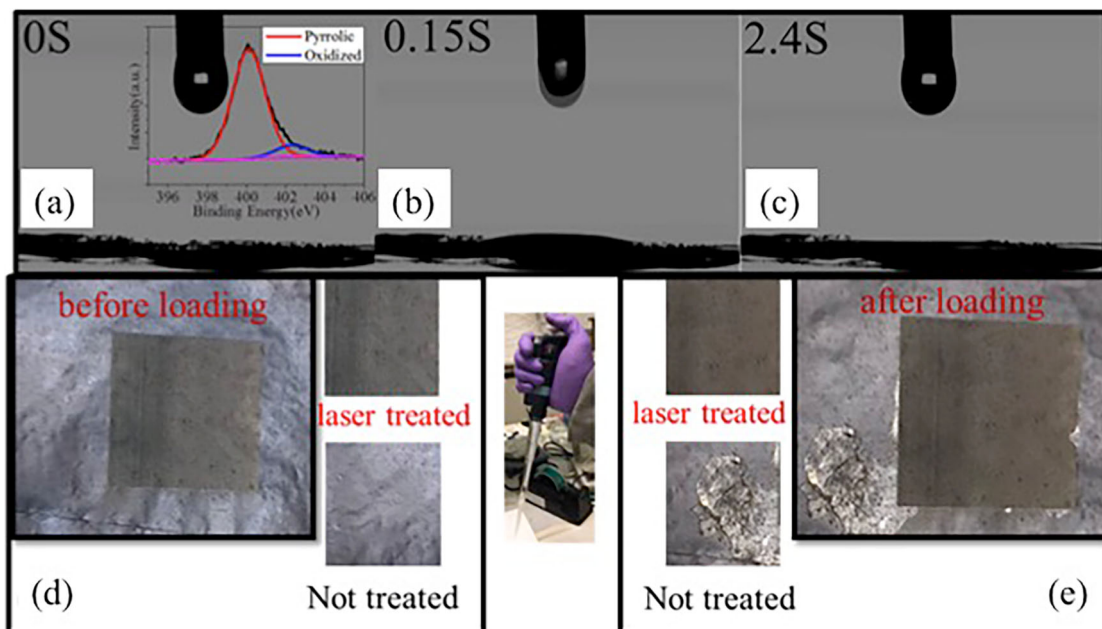
Fig. 4 An overview of the cross-linked sulfur loading on laser synthesized cathode. a–c spread of the cross-linked sulfur droplet on super-hydrophilic nitrogen doped graphene with nano-MoS$_2$ from 0 to 2.4 s, **d** cathode surface before sulfur loading and **e** cathode surface after sulfur loading.

linked sulfur with styrene (15% styrene and 85% sulfur) dissolved in CS$_2$, and then was loaded at 65% content on the doped graphene with nano-MoS$_2$ loading[18]. As shown in Fig. 2c, the confined sulfur in cross-linked organic structures was attracted by the polar metal sulfide–MoS$_2$ particles and surround nanoparticles.

**Charge/discharge performance and electrochemical properties.**
The heteroatom doped porous graphene with nano-MoS$_2$ loading (black squares in Fig. 5) enabled a high gravimetric capacity of 1310 mAhg^{-1} at 0.1 C (discharge/charge of full theoretical capacity in 20 h) charge rate, as shown in Fig. 5a. After 5 cycles, the capacity stabilized to 1150 mAhg^{-1}, which was about 1.2 times that of laser synthesized doped graphene mixed with micro-MoS$_2$ particles and was about 2.3 times of capacity that of cross-linked S/heteroatom doped porous graphene without MoS$_2$ (blue squares). The same mass of the nano-MoS$_2$ in the heteroatom doped graphene had more active surface area that can fasten more elemental sulfur. At 0.5 C the initial discharge capacity of laser synthesized doped graphene with micro-MoS$_2$ was 670 mAhg^{-1}, 685 mAhg^{-1} presented similar capacity after 500 cycles as shown in Fig. 5b. Much higher 2 and 3 C charge rates were applied and the results both showed a reduced trend in 100 cycles and reverse back to the original capacities or even higher shown in Fig. 5c, although the columbic efficiency dropped gradually, since the diffusion effect could not be eliminated. In Fig. 5(d, e), the faster reaction kinetics QL/QH solid-state diffusion (QH is the capacity contributions of high-order polysulfide conversion from 2.6 to 2.3 V and QL is that of the low-order polysulfide conversion from 2.1 to 1.9 V) and higher order Li$_2$Sx diffusion in the second plateau with 0.5 C rate led to the value of QL/QH < 3 and the more active surface area from nano-MoS$_2$ reduced effect[38]. As the current density increased from 0.1 to 1 C, the heteroatom doped porous graphene with nano-MoS$_2$ implant electrode displayed recoverable and stable capacities from 1310 mAhg^{-1} for 0.1 C to 600 mAhg^{-1} for 1 C charge rate. A stable capacity of 445 mAhg^{-1} remained even at high current density of 3 C was obtained. When the current rate gradually returned to 0.5 and 0.1 C, the capacity recovered back to 775 and 1212 mAhg^{-1}, respectively. As the

current density increased from 0.1 to 1 C the pure heteroatom doped porous graphene electrode and that with micro-MoS$_2$ particles were capable to recover their capacity and keep stable from 1296 to 443 mAhg^{-1} and 560 to 206 mAg^{-1}, respectively. At 0.5 C, the initial discharge capacity of laser synthesized doped graphene with nano-MoS$_2$ was 768 mAhg^{-1}, a considerably low fading rate 0.002% sustained 760 mAhg^{-1} after 500 cycles (Fig. 5b).

The N and S doped porous laser-induced graphene structure presented enhanced interface adsorption, which suppressed diffusion of polysulfide into the electrolyte.

Figure 6 shows the Nyquist plot of the Li–S battery internal impedance derived from electrical impedance spectroscopy, and an equivalent circuit model for the battery. The internal resistances of various parts are shown in Fig. 7. The transport pathway and initial Re—the resistance of electrolyte shown in Fig. 7 for both ions and electrons in the electrolyte were reduced to 4–5 ohm, because of the low surface energy of hydrophilic surface shown in the Figure[32,37]. Hence, it enabled the stable charge performances during the changes of the current density from 0.1 to 3 C. The ΔE (0.1 V) in Fig. 5d, e of electrochemical polarization induced stable and high columbic efficiency over 97%, which was due to the functionalized porous laser synthesized graphene with nitrogen doping. During the 40 cycles, the laser induced graphene with nanoparticles (black squares) in Fig. 5a had slightly higher and more stable coulombic efficiency than both the laser induced graphene mixed with the micro-MoS$_2$ particles and that of graphene without an active metal.

At 500 cycles, the resistance of electrolyte R_e, remained at similar values of 4.4 Ohm for the laser synthesized doped graphene with micro-MoS$_2$ before 300 cycles and a small inflation from 4.4 to 4.8 Ohm with 200 more cycles was due to polysulfide diffusion (Fig. 7). Low fluctuation around 4.2 Ohm with nano-MoS$_2$ in 500 cycles presented a more stable performance of the electrolyte shown in Fig. 7. R_{int} is the interphase contact resistance, which is related to the electron conduction from bulk free radical sulfur. Both R_{int} of laser synthesized dope graphene electrodes with nano-MoS$_2$ and micro-MoS$_2$ increased to 8 and 14 Ohm, respectively at the
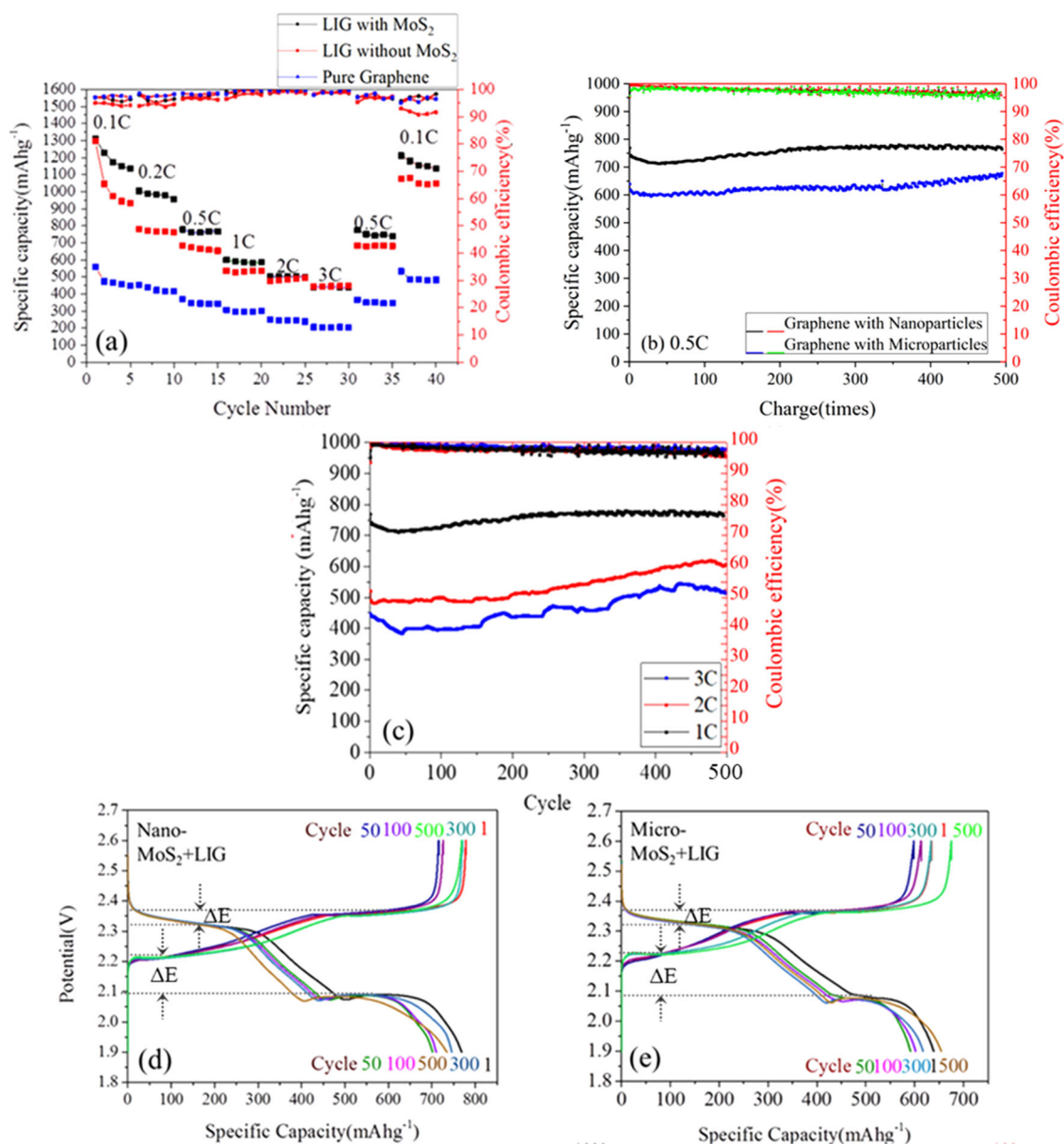
Fig. 5 Electrochemical performance of the laser induced cathode. a Rate capacities of the N/S doped laser synthesized doped graphene (LIG) with and without MoS_2 particles. **b** Long-term cycles and Coulombic efficiency of the electrodes with nano and micro MoS_2 particles at a 0.5 C charge rate. **c** Charge capacities (1, 2, and 3 C) for long-term cycles and Coulombic efficiency of the electrodes with nano MoS_2 particles. **d** 1, 50, 100, 300, and 500 cycle charge and discharge profiles for electrodes with nano MoS_2 particles and **e** cycle charge and discharge profiles for electrodes micro MoS_2 particles.

beginning. This was attributed to the rearrangement of sulfur particles as electrochemical reaction procedures. Afterwards, R_{int} dropped to 2–3 Ohm in 500 cycles. Compared with R_{int} of, laser synthesized doped graphene electrode with nano-MoS_2, the value of R_{int} with micro-MoS_2 presented a fluctuation from 3 to 6 Ohm in 100 cycles. R_{ct} is the charge-transfer resistance and related capacitance between conductive agent and electrolyte. After 500 cycles, R_{ct} of the laser synthesized doped graphene electrodes with nano-MoS_2 and micro-MoS_2 were lower than 2.5 Ohm. The fluctuation of laser synthesized doped graphene electrodes with micro-MoS_2 also existed in first 100 cycles. The fluctuation of R_{ct} and R_{int} could be ascribed to the production of nonconductive reduction Li_2S_2–Li_2S. In Fig. 5b, the capacity of laser synthesized doped graphene electrodes with micro-MoS_2 had a more clearly reduced trend in the first 100 cycles and reverse back to the original capacity, which was related to the change of R_{int} and R_{ct}. This phenomenon was

related to the functionalized laser synthesized doped graphene electrodes with pyrrolic N doping. It can promote oxygen-containing functional groups chemically bonding with sulfur. The sulfur atom is more thermodynamically favorable to the lower interaction energy of pyrrolic than carbon. The higher electronegativity of nitrogen(3.0) induced polarization of nearby oxygen containing groups and was more easily attacked by sulfur atoms than that of carbon at 155 °C[39]. Li^+ with more negative charge was easier adsorbed on N with more positive charge, which bonded with more negative oxygen functional group with self-extra electron transfer. Pyrrolic process can transfer extra electron to oxygen containing groups, which leads to stronger ionic bonding with Li^+[40]. Thus, after 100 cycles, a slightly higher R_{ct} and R_{int} enabled the internal circumstance of the cell to recapture the lost polysulfide (Li_2S_4 to Li_2S_6) in electrolyte gradually by co-ionic attractions from MoS_2 particles and N doped graphene in the rest 400 cycles.
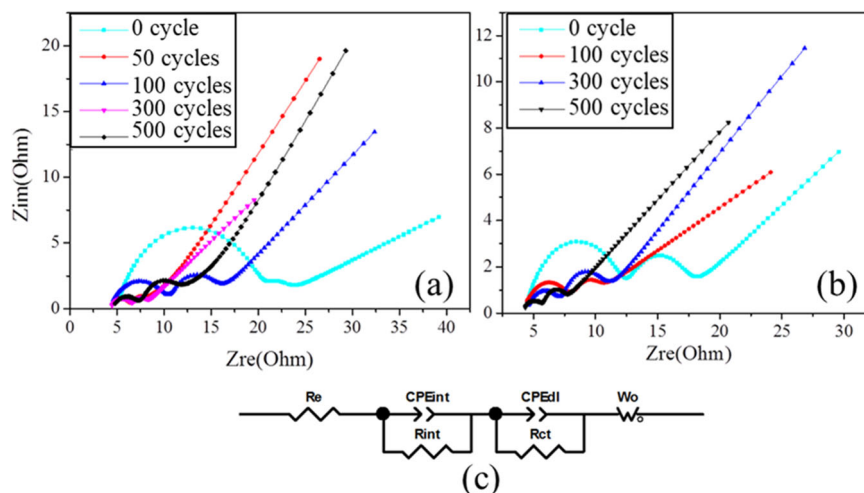
Fig. 6 Electrochemical characterization. Nyquist plots of the Li–S battery at same depth of discharge (2.3 V) but different cycles (100–500) for electrodes: **a** N/S doped laser synthesized doped graphene (LIG) with micro-MoS$_2$ loading, **b** N/S doped laser synthesized doped graphene (LIG) with nano-MoS$_2$ loading and **c** proposed equivalent circuit for cell.
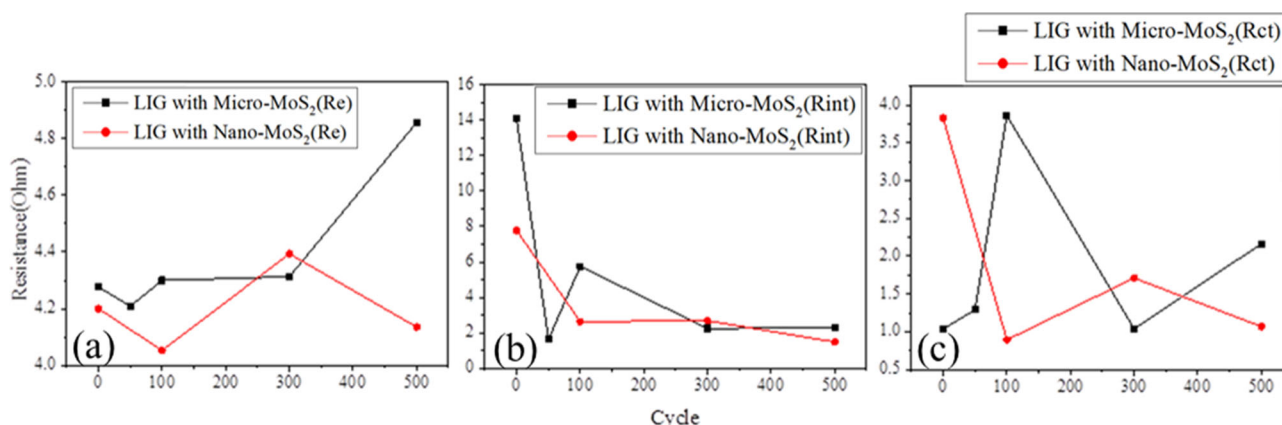
Fig. 7 Internal resistances of the Li-S battery. Plots of various electrical resistance **a** electrolyte resistance (Re), **b** interphase contact resistance (Rint), and **c** charge-transfer resistance (Rct) against the charge/discharge cycles from 0 to 500 for LIG with Nano/Micro MoS$_2$.

Mechanism of charge/discharge cycle stability. The function of heteroatom doped laser synthesized electrodes with MoS$_2$ loading on lithium (poly)sulfides on electrode was determined from S 2p X-ray photoelectron core level spectrum. The results are summarized in Fig. 8. The imide-based salt at 169.3 eV and –SO$_4$ are originated from the LiTFSI addition in electrolyte[41]. The Li$_2$S$_2$ at 161.6 eV is remained from discharge/charge procedure. Li$_2$S$_4$–Li$_2$S$_6$ was representative polysulfide at a 2.3 V partial state of discharge[42]. Its XPS spectrum shows a 21–23% sulfur content at the range of 163–164 eV for laser synthesized doped graphene electrodes with nano-MoS$_2$ in entire sulfur system during 500 cycles discharge/charge. The 15–19% content for laser synthesized doped graphene electrodes with micro-MoS$_2$ was much lower than that of nano-MoS$_2$ that had higher active surface areas. The loss of polysulfide diffusing in electrolyte was limited after 500 cycles discharge/charge under the system of laser synthesized doped graphene electrodes with MoS$_2$ and cross-linked sulfur loading. The attacks between S and oxygen containing content generated the product from –SO$_2$ signal at 165.6 eV, whose bond supported the capacity recapture and high stability mechanism.

An in situ generation of heteroatom (N and S) doped graphene with nano-MoS$_2$ particle loading on the battery electrodes by laser direct writing technique formed a Li–S cell cathode without a binder, which achieved considerably low R_{int} (<3 Ohm) and R_{ct}

(<2.5 Ohm) after 500 discharge/charge cycles. We demonstrated that a Li–S cell with a charge capacity decay as low as 0.002% per cycle over 500 cycles and even increasing the charge capacity over long cycles could be achieved by using the system with pyrrolic N doping, nano/micro-MoS$_2$ particles loading and cross-linked sulfur. The ionic bond attraction from pyrrolic N doping and MoS$_2$ recaptured and refastened the charge capacity from diffused polysulfide after 100 cycles.

Methods

Preparation of an organic ink for laser synthesis of doped graphene with MoS$_2$ particle loading. Poly[2,2′-(m-phenylen)−5,5′-bisbenzimidazole (PBI) was dissolved in DMSO, (CH$_3$)$_2$SO at a 10% PBI concentration prepared with 4 h stirring at 60 °C, then 50% weight mass MoS$_2$ micro-particles (50–60 μm in size, from Sigma) was mixed in the PBI ink with 30 min stirring. A layer of above solution was coated on an aluminum foil with a 100 μm space doctor blade and 30 min drying in furnace at 80 °C. In a different experiment, a layer of PBI with DMSO was coated on a polyethylene terephthalate (PET) film with a 100 μm space doctor blade and 30 min drying in furnace at 80 °C.

Laser direct synthesis of battery electrode. Laser direct writing in ambient condition was carried out using an Edgewave picosecond laser (a 10 ps pulse with operating at 355 nm laser wavelength) with a laser fluence of 13 mJ cm^{-2}, a pulse repetition rate of 3372.8 kHz, and a scanning speed of 100 mm s^{-1} using a galvo x–y scanner. The focused beam spot size was 40 μm on the coating surface. The laser beam scanning line spacing was 0.02 mm. The ablation of MoS$_2$ microparticle by the picosecond laser and
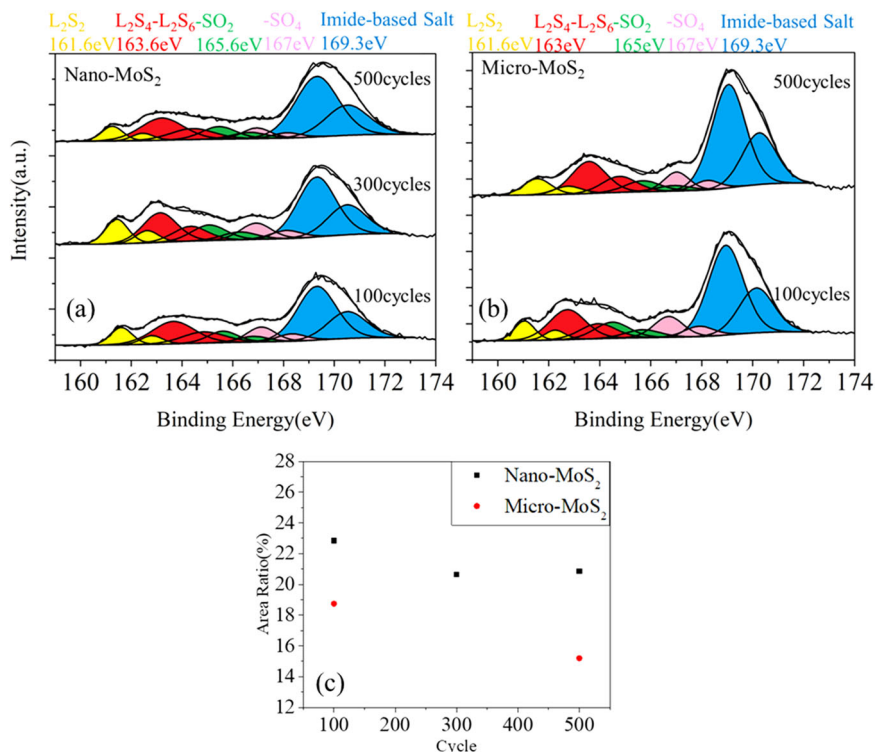
Fig. 8 XPS spectra of various materials produced. a Laser synthesized N/S doped graphene with nano-MoS$_2$, **b** laser synthesized N/S doped graphene with micro-MoS$_2$, and **c** ratio between polysulfide and imide-based salt from LiTFSI after charge/discharge for 100, 300, and 500 cycles at the same charge voltage (2.3 V).

self-generated protection gas from the organic ink induced 30% nanoparticle MoS$_2$ implant, as shown in the thermal gravimetric analysis (TGA) later in this paper, in laser synthesized doped graphene structure.

Preparation and loading of reverse vulcanized sulfur solution. S$_8$ (5 g, 156 mmol) and styrene (0.88 g, 8.47 mmol) were stirred and copolymerized at 130 °C for 4 h. The light orange solid poly (sulfur-styrene) was dissolved in the CS$_2$ solution at 5% concentration.

For laser synthesized doped graphene with nanoparticle MoS$_2$ electrode, 43.7 mg of the above solution (1 mg/cm^{-2}) was spread on each laser processed cathode by a micropipette in a 65:35 mass ratio. Then CS$_2$ was removed in an 80 °C furnace for 30 min. For laser synthesized doped graphene with microparticulate MoS$_2$ electrode, poly (sulfur–styrene) solution was mixed in 65:14:16:5 mass ratio with the MoS$_2$ micro-particle, the laser synthesized S and N doped graphene was collected from the PET film and a water soluble binder carboxymethyl cellulose/styrene–butadiene rubber. Then, it was coated on an 20 µm aluminum foil with a 100 µm space doctor blade and 30 min drying in furnace at 80 °C.

Electrochemical measurement procedure. Electrochemical studies were carried out using a BaSyTec CTS system in galvanostatic mode for charge cycles up to 500 cycles for the 0.5 to 3 C charge rates and IviumStat for electrochemical impedance measurements in a frequency range between 100 mHz and 100 kHz with a perturbation amplitude of 5 mV, employing electrodes in coin cells with a lithium foil as the anode and Celgard 2400 sheets. Cells were operated in a charge voltage window of 1.9–2.6 V in an electrolyte comprising 1 M of LiTFSI in a 1:1 volume of dimethyl ether (DME,C$_2$H$_3$OCH$_3$): Dioxolane (DOL,(CH$_2$)$_2$O$_2$CH$_2$) and 2 wt% LiNO$_3$.

Material characterization procedure. The laser synthesized electrodes were analyzed using Raman spectrometry with a single excitation wavelength of 514 nm. TGA was used to determine the MoS$_2$ nanoparticle content on the electrode employing a heating rate of 5 °C/min from room temperature to 800 °C under ambient condition. Field Emission Gun—Scanning Electron Microscopy (FEG-SEM, Zeiss Merlin SEM with Gemin II), Scanning Transmission Electron Microscopy (TEM, Talos F200X) at 200 keV, X-ray Photoelectron Spectroscopy (XPS) analysis were used to understand the atomic structures and chemical reactions in the Li-S battery after cycles. XPS experiments were performed using the Kratos Axis Ultra facility equipped with a monochromatic Al K X-rays source. The high resolution core levels spectra were acquired at a pass energy of 20 eV by a hemi-spherical energy analyzer positioned along the surface normal. Spectra were calibrated by assigning a binding energy value of 689 eV to the CF$_2$ component of 1 s

core level to F XPS core level profiles were fitted with CasaXPS software employing the Gaussian–Lorentzian lineshape.

Data availability
The datasets generated during the current study are available from the corresponding author on reasonable request.

References
1. Whittingham, M. S. History, evolution, and future status of energy storage. *Proc. IEEE* **100**, 1518–1534 (2012).
2. Scrosati, B. History of lithium batteries. *J. Solid State Electrochem.* **15**, 1623–1630 (2011).
3. Chen, Y. M., Yu, X. Y., Li, Z., Paik, U. & Lou, X. W. Hierarchical MoS2 tubular structures internally wired by carbon nanotubes as a highly stable anode material for lithium-ion batteries. *Sci. Adv.* **2**, e1600021 (2016).
4. Ye, R. et al. Advanced sulfur-silicon full cell architecture for lithium ion batteries. *Sci. Rep.* **7**, 17264 (2017).
5. Lu, J. S., Maggay, I. V. B. & Liu, W. R. CoV2O4: a novel anode material for lithium-ion batteries with excellent electrochemical performance. *Chem. Commun.* **54**, 3094–3097 (2018).
6. Fang, R. P. et al. More reliable lithium-sulfur batteries: status, solutions and prospects. *Adv. Mater.* **29**, 1606823–1606847 (2017).
7. Zhang, J. et al. Nanostructured host materials for trapping sulfur in rechargeable Li-S batteries: structure design and interfacial chemistry. *Small Methods* **2**, 1700279–1700310 (2018).
8. Yin, Y. X., Xin, S., Guo, Y. G. & Wan, L. J. Lithium-sulfur batteries: electrochemistry, materials, and prospects. *Angew. Chem. Int. Ed.* **52**, 13186–13200 (2013).
9. Su, Y. S. & Manthiram, A. Lithium-sulphur batteries with a microporous carbon paper as a bifunctional interlayer. *Nat. Commun.* **3**, 1166 (2012).
10. Sun, L. et al. Super-aligned carbon nanotube/graphene hybrid materials as a framework for sulfur cathodes in high performance lithium sulfur batteries. *J. Mater. Chem. A* **3**, 5305–5312 (2015).

11. Yang, X., Li, X., Adair, K., Zhang, H. & Sun, X. Structural design of lithium–sulfur batteries: from fundamental research to practical application. *Electrochem. Energy Rev.* **1**, 239–293 (2018).

12. Balach, J., Linnemann, J., Jaumann, T. & Giebeler, L. Metal-based nanostructured materials for advanced lithium-sulfur batteries. *J. Mater. Chem. A* **6**, 23127–23168 (2018).

13. Jayaprakash, N., Shen, J., Moganty, S. S., Corona, A. & Archer, L. A. Porous hollow carbon@sulfur composites for high-power lithium-sulfur batteries. *Angew. Chem. Int. Ed.* **50**, 5904–5908 (2011).

14. He, B., Li, W.-C., Yang, C., Wang, S.-Q. & Lu, A.-H. Incorporating sulfur inside the pores of carbons for advanced lithium–sulfur batteries: an electrolysis approach. *ACS Nano* **10**, 1633–1639 (2016).

15. Zhou, W., Xiao, X., Cai, M. & Yang, L. Polydopamine-coated, nitrogen-doped, hollow carbon–sulfur double-layered core–shell structure for improving lithium–sulfur batteries. *Nano Lett.* **14**, 5250–5256 (2014).

16. Zheng, G., Yang, Y., Cha, J. J., Hong, S. S. & Cui, Y. Hollow carbon nanofiber-encapsulated sulfur cathodes for high specific capacity rechargeable lithium batteries. *Nano Lett.* **11**, 4462–4467 (2011).

17. Zang, J. et al. Hollow-in-hollow carbon spheres with hollow foam-like cores for lithium–sulfur batteries. *Nano Res.* **8**, 2663–2675 (2015).

18. Zhang, Y. Y. et al. Inverse vulcanization of elemental sulfur and styrene for polymeric cathodes in Li-S batteries. *J. Polym. Sci. Pol. Chem.* **55**, 107–116 (2017).

19. Zhang, Y. Y. et al. Nucleophilic activation of elemental sulfur for inverse vulcanization and dynamic covalent polymerizations. *J. Polym. Sci. Pol. Chem.* **57**, 7–12 (2019).

20. Zhang, Y. Y. et al. Functionalized chalcogenide hybrid inorganic/organic polymers (CHIPs) via inverse vulcanization of elemental sulfur and vinylanilines. *Polym. Chem.* **9**, 2290–2294 (2018).

21. Smith, J. A., Wu, X. F., Berry, N. G. & Hasell, T. High sulfur content polymers: the effect of crosslinker structure on inverse vulcanization. *J. Polym. Sci. Pol. Chem.* **56**, 1777–1781 (2018).

22. Simmonds, A. G. et al. Inverse vulcanization of elemental sulfur to prepare polymeric electrode materials for Li-S batteries. *ACS Macro Lett.* **3**, 229–232 (2014).

23. Griebel, J. J. et al. Dynamic covalent polymers via inverse vulcanization of elemental sulfur for healable infrared optical materials. *ACS Macro Lett.* **4**, 862–866 (2015).

24. Wu, R. et al. Hierarchically porous nitrogen-doped carbon as cathode for lithium-sulfur batteries. *J. Energy Chem.* **27**, 1661–1667 (2018).

25. Liang, X. et al. A highly efficient polysulfide mediator for lithium-sulfur batteries. *Nat. Commun.* **6**, 5682 (2015).

26. Ji, P. H., Shang, B., Peng, Q. M., Hu, X. B. & Wei, J. W. alpha-MoO3 spheres as effective polysulfides adsorbent for high sulfur content cathode in lithium-sulfur batteries. *J. Power Sources* **400**, 572–579 (2018).

27. Cui, Z. M., Zu, C. X., Zhou, W. D., Manthiram, A. & Goodenough, J. B. Mesoporous titanium nitride-enabled highly stable lithium-sulfur batteries. *Adv. Mater.* **28**, 6926–6931 (2016).

28. Peng, H. J., Huang, J. Q. & Zhang, Q. A review of flexible lithium-sulfur and analogous alkali metal-chalcogen rechargeable batteries. *Chem. Soc. Rev.* **46**, 5237–5288 (2017).

29. Liang, X. et al. A facile surface chemistry route to a stabilized lithium metal anode. *Nat. Energy* **2**, 17119 (2017).

30. Liu, D. H. et al. Catalytic effects in lithium-sulfur batteries: promoted sulfur transformation and reduced shuttle effect. *Adv. Sci.* **5**, 1700270 (2018).

31. Liang, J. et al. Kinetically enhanced electrochemical redox of polysulfides on polymeric carbon nitrides for improved lithium-sulfur batteries. *ACS Appl Mater. Interfaces* **8**, 25193–25201 (2016).

32. Huang, Y. et al. Laser direct writing of heteroatom (N and S)-doped graphene from a polybenzimidazole ink donor on polyethylene terephthalate polymer and glass substrates. *Small* **14**, 1803143 (2018).

33. Lin, J. et al. Laser-induced porous graphene films from commercial polymers. *Nat. Commun.* **5**, 5714 (2014).

34. Wang, L. et al. Formation of deep-subwavelength structures on organic materials by femtosecond laser ablation. *IEEE J. Quantum Electron.* **54**, 1–7 (2018).

35. Arnold, N. & Bityurin, N. Model for laser-induced thermal degradation and ablation of polymers. *Appl. Phys. A* **68**, 615–625 (1999).

36. Yan, J. W., Noguchi, J. & Terashi, Y. Fabrication of single-crystal silicon micro pillars on copper foils by nanosecond pulsed laser irradiation. *Cirp Ann.* **66**, 253–256 (2017).

37. Xu, G. Y. et al. High performance lithium-sulfur batteries: advances and challenges. *J. Mater. Chem. A* **2**, 12662–12676 (2014).

38. Gueon, D. et al. Spherical macroporous carbon nanotube particles with ultrahigh sulfur loading for lithium-sulfur battery cathodes. *ACS Nano* **12**, 226–233 (2018).

39. Song, J. et al. Nitrogen-doped mesoporous carbon promoted chemical adsorption of sulfur and fabrication of high-areal-capacity sulfur cathode with exceptional cycling stability for lithium-sulfur batteries. *Adv. Funct. Mater.* **24**, 1243–1250 (2014).

40. Song, J. et al. Strong lithium polysulfide chemisorption on electroactive sites of nitrogen-doped carbon composites for high-performance lithium–sulfur battery cathodes. *Angew. Chem. Int. Ed.* **54**, 4325–4329 (2015).

41. Sharova, V. et al. Comparative study of imide-based Li salts as electrolyte additives for Li-ion batteries. *J. Power Sources* **375**, 43–52 (2018).

42. Pang, Q., Liang, X., Kwok, C. Y. & Nazar, L. F. Review—the importance of chemical interactions between sulfur host materials and lithium polysulfides for advanced lithium-sulfur batteries. *J. Electrochem. Soc.* **162**, A2567–A2576 (2015).

Author contributions
Y.H., Q.C., and G.Z. designed and manufactured the experimental specimen. Y.H. and R. F. carried out the electrochemical performance experiments. Y.H., Y.P., and H.Z. carried out the SEM and TEM analysis. M.S.W. and Y.H. carried out the XPS analysis. Y.H. drafted the initial paper. L.L. directed and technically supervised this study and edited the paper. Z.L. supervised the material science aspects of the project.

Competing interests
The authors declare no competing interests.

Additional information
Correspondence and requests for materials should be addressed to L.L.

Reprints and permission information is available at http://www.nature.com/reprints

Publisher's note Springer Nature remains neutral with regard to jurisdictional claims in published maps and institutional affiliations.